

Article

Laser Beam Welding of CubeSat 1U Structure Parts Obtained by Powder Bed Fusion

Rafael Humberto Mota de Siqueira ¹, Diego Javier Celentano ² and Milton Sergio Fernandes de Lima ^{1,*}

¹ Photonics Division, Institute for Advanced Studies, Trevo Amarante 1, Sao Jose dos Campos 12228-001, SP, Brazil

² Department of Mechanical and Metallurgical Engineering, Pontifical Catholic University of Chile, Avda. Vicuña Mackenna, Santiago 4860, Chile

* Correspondence: miltonmsfl@fab.mil.br; Tel.: +55-12-3947-5464

Abstract: This study contributes to a possible methodology for manufacturing CubeSats using additive manufacturing and laser beam welding. Titanium connectors were constructed by selective laser melting and electron beam melting and characterized from a topological point of view. The connectors can be joined to titanium tubes for the construction of CubeSats via laser spot welding. The fiber laser welds exhibited full penetration using pulses with 400 J of energy. The welds showed titanium acicular martensite grains with recesses and pores. The average hardness of the cast zone was 350 HV, which is close to the hardness of the connectors (400 HV) and more rigid than that of the tubes (100 HV). Spot welding has proven to be useful in resisting forces above 2000 N, which is sufficient for CubeSat frame space applications.

Keywords: laser materials processing; laser beam welding; titanium alloys; space structures



Citation: Siqueira, R.H.M.d.; Celentano, D.J.; Lima, M.S.F.d. Laser Beam Welding of CubeSat 1U Structure Parts Obtained by Powder Bed Fusion. *Metals* **2022**, *12*, 1992. <https://doi.org/10.3390/met12111992>

Academic Editor: Aleksander Lisiecki

Received: 2 November 2022

Accepted: 18 November 2022

Published: 21 November 2022

Publisher's Note: MDPI stays neutral with regard to jurisdictional claims in published maps and institutional affiliations.



Copyright: © 2022 by the authors. Licensee MDPI, Basel, Switzerland. This article is an open access article distributed under the terms and conditions of the Creative Commons Attribution (CC BY) license (<https://creativecommons.org/licenses/by/4.0/>).

1. Introduction

In recent years, there has been a marked increase in the interest in space exploration [1]. Several missions have been carried out and are still currently under development, expanding the frontier of human presence in space in a way that has never been seen before. According to forecasts by the website specializing in nanosatellites [2], by the end of 2022, there should be approximately 646 nanosatellites in orbit, a record since the beginning of operations in 1998 and twice as many as in 2021. The United States of America leads a number of constellations with 54% of the satellite constellations, followed by the European Community with 26%. Currently, 86% of all nanosats are CubeSat compositions, with an emphasis on the 3U configuration, that is, the composition of three cubes of 1 L volume each.

The construction of satellites is extremely complex and subject to high risks, and the present study intends to contribute to a small part of this area with a methodology for the construction of titanium CubeSat structures. The CubeSat frame can be designed in a range of materials, from polymers to metals, with characteristics that meet mission requirements [3]. However, metallic structures have proven useful in withstanding extreme launches and operating conditions. For example, Nano Avionics US LLC (Columbia, IL) produces a series of aluminum alloy frames, class 7075-T7351, for CubeSats [4]. NASA has developed a number of suppliers of aluminum CubeSat primary structures, with the aluminum alloys 6061 or 7075, which have proven to be reliable and stable in the conditions of wide temperature variations in space [5]. The use of titanium in the construction of CubeSats is less well known, with reports of its use in stabilization and propulsion systems, particularly in N₂H₄ tanks [6].

Several manufacturing processes have been applied in the construction of space structures, and additive manufacturing (AM) is currently one of the most promising tools [7]. In general, additive manufacturing does not lend itself well to the construction of

large finished products. The time and costs involved would be extremely high, and the examples available in the market are just proofs of concept and, except for rare excesses, are not relevant in the manufacturing scenario. As examples, turbine blades by directed energy deposition AM have been repaired [8], and cooling channels by AM in plastic injection molds have been constructed [9]. This is also the case in the present study of CubeSat structures, as it is not logical to build an integral structure using AM [10]. On the other hand, connectors are somewhat customizable and can be joined to supporting structures at the edges produced by conventional means. Two AM techniques are competitive for titanium parts: selective laser melting (SLM) and electron beam melting (EBM) [11]. Therefore, this study analyzed both alternatives.

Few authors have studied the union between the parts manufactured conventionally and those by AM. The specific case of titanium components is even more limited. For example, Yu et al. [12] reported some results on SLM parts joined to wrought Ti-6Al-4V by laser beam welding (LBW). The authors utilized a fiber laser with a power of 4 kW and welding speeds between 1 and 2 m/min to weld two 5 mm plates, wrought, and SLM plates. The fusion zone is marked by acicular α' martensite inside the prior β grains. The hardness reached 450 HV in the fusion zone and was slightly depleted in the heat-affected zone.

The objective of the present study is to investigate whether SLM and EBM connectors can be properly joined via LBW to titanium tubes as an original contribution to the CubeSat designs.

2. Materials and Methods

Figure 1a shows a three-way tube connector that is to be built using SLM and EBM. The typical dimensions of a cross-sectional cut are presented in Figure 1b. The computer model was designed in Solid Works[®] version 2022 (Dassault Systèmes, France), and slicing was performed in AM machines.

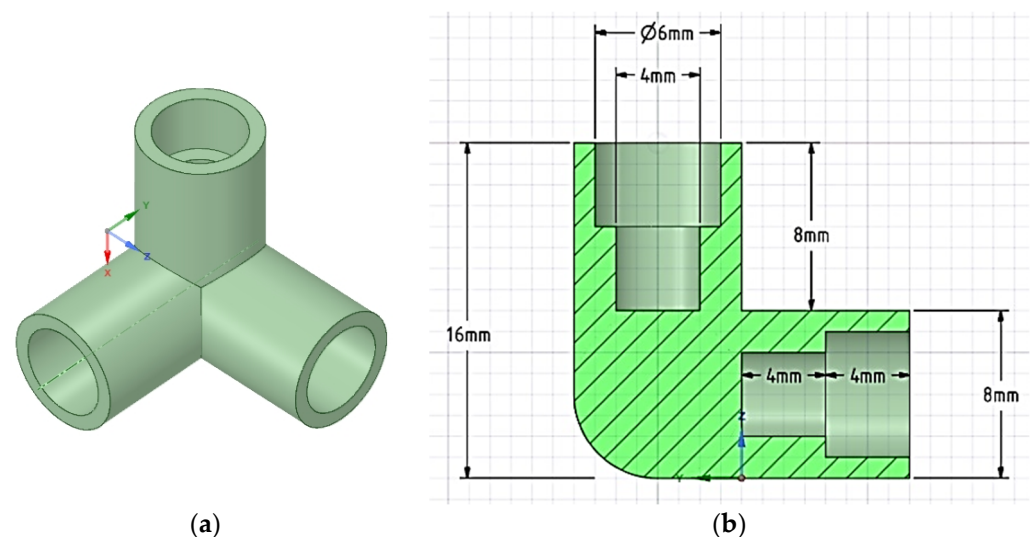


Figure 1. Computer drawing of the connector (a) and its dimensions (b).

The powders used in the SLM and EBM processes had a composition of Ti6Al4V alloy (Ti, 5.72%Al, 4.1%V, 0.37%Fe, 0.065%C, 0.04%N, 0.15%O, 0.013%H, by weight), as given by the powder fabricant. Spherical particles of the powder were sieved to obtain a granulometric distribution between 45 and 60 μm .

SLM was performed on an EOS M280 instrument (Krailing, Germany) using a laser power of 170 W and a process speed of 1350 mm/s. Each layer was applied by rotating the previous layer by 60° to mitigate anisotropy, with a thickness of 30 μm each and a

distance between the lines of 0.1 mm. The process chamber was filled with argon at ambient pressure after purging to eliminate atmospheric gas.

The EBM equipment was a GE ARCAM Q10 (West Chester, PA, USA) with an electron source of a current of 41 mA and a voltage of 60 keV. In the focal plane, the estimated current was 3.073 mA. After purging with pure argon, the chamber was evacuated to 3.9 kbar after a purge with pure argon. The process speed was set to 8000 mm/s, and the powder bed was preheated to 560 °C before the start of growth. The different processing speeds for SLM and EBM are due to the in-built recipes in the models and could not be changed, although this parameter could change the quality of the built volume.

The connectors built by SLM and EBM were laser-welded to commercially pure grade 2 titanium tubes to compose a cube of 1 L volume. The tubes that made up the edges of the cube had an outer diameter of 6 mm and a wall thickness of 1 mm. The connectors and tube were designed to minimize the weight of the assembly. The maximum permissive gap tube to the connector terminal is 0.5 mm.

For the LBW, IPG Photonics YLR2000 (Oxford, MA, USA) equipment with a maximum power of 2 kW and a minimum focal diameter of 0.1 mm was used. The welding strategy involves laser spot welding on one side of the connector to the tube to join the three tubes in each connector until the complete formation of the structure is reached. Each spot weld was performed 3 mm from the edge with a power of 1 kW per shot and a beam diameter of 7.4 mm. The pulse temporal length was 400 ms; therefore, each laser shot had an energy of 400 J and an energy density of 9.3 J/mm². A shielding gas nozzle blasted 10 L/min of pure argon during the spot welding.

The density measurements of the connectors were obtained using the Archimedes method, according to ASTM C373-18 [13]. For the measurements, a Shimadzu analytical balance model AUX320 was used. The dry angle mass was measured after the angle was maintained in a muffle furnace at 50 °C for 5 h. To measure the submerged mass, the connector was first placed in a beaker with distilled water and heated at 100 °C for 5 h. At the end of the time that the connector was kept at 100 °C, the heating was turned off, and the sample was left in a beaker with water for 24 h before the mass was measured. The saturated mass was measured after the submerged mass was measured. As the connectors were removed from the beaker with water, the excess water was dried with absorbent paper, and the mass was measured.

Optical microscopy (OM) was performed using a Zeiss microscope Axio Imager.A2m (Oberkochen, Germany). Microstructural analysis was performed on the samples, which were cut on a metallographic saw with a diamond disk with a constant lubrication and on Bakelite synthetic resin. The sanding process was carried out in a motorized sander at a speed of 300 rpm, with silicon carbide water sandpaper of 220, 320, 400, 600, 800, 1200, 1500, and 2000 grit. at a speed of 600 rpm and a diamond paste with a granulometry of 6 µm, 3 µm, and 1 µm. Final polishing was performed using colloidal silica. To visualize the microstructure, after polishing the samples were etched with Kroll reagent (10 mL of HF, 45 mL of HNO₃, and 45 mL of H₂O) for 30 s, washed in water, and dried with a jet of compressed air. The etching methodology was based on ASTM E 407-99 [14].

The real piece was compared with the electronic model of the connector using 3D scanning of the part after fabrication. Three-dimensional scanner equipment of the brand GOM model ATOS Triple Scan was used; it offered 16,924 measurement points with a resolution of 20 nm. The results allowed for the determination of the maximum and minimum differences between the real and electronic surfaces of the model in relation to the normal of their surfaces.

Roughness analysis was performed using a Leica confocal microscope (DCM3D). A roughness analysis was performed to measure the difference in surface finish between the connectors produced by SLM and EBM. As reported in the literature, there are differences in the surface finish of parts produced by SLM and EBM [15].

The Vickers microhardness test was used to measure the variation in the hardness values of the two samples analyzed in different regions. The Vickers microhardness tests

were performed using a Future-Tech microhardness meter, model FM-700. The load used in the tests was a 100 g force (gf), with a load application time of 10 s, and with the aid of a microscope coupled to the microhardness meter, the diagonals of the impression were measured, and the equipment provided toughness values. The samples used for mapping the hardness profile were the same as those used in the microstructural analyses. Therefore, the samples were embedded, sanded, polished, and etched. The samples to be tested were positioned in a microdurometer such that the weld bead was perpendicular to the indentation line. The first indentation was performed on the angle towards the weld bead until it reached the tube, maintaining a spacing between the indentations of 0.05 mm.

Tensile strength tests were carried out in the universal testing machine Emic, model DL 100 kN, with a maximum capacity of 10,000 kgf and a bench speed of 1 mm/min, at room temperature.

3. Results and Discussions

3.1. Characterization of the AM Connectors

Initially, connectors obtained by additive manufacturing should be characterized from a metrological point of view. Figure 2a,b shows the 3D mapping of the connectors obtained by SLM (a) and EBM (b), respectively. Considering the vector moduli, the SLM real dimensions deviate from the electronic model in the range from -0.242 mm (minimum) to $+0.145$ mm (maximum). The EBM measurements indicated a deviation of -0.179 mm (minimum) to $+0.130$ mm (maximum). As the tolerances are quite large, with an approximately 0.5 mm tube-to-flange gap, the solids reproduced the idealized connector from the CAD quite well, independently of the heat source. Figure 2c,d presents the actual connectors. As can be seen, both the SLM and the EBM presented the required design for the purpose. The surface aspect is granular, and the SLM aspect seems to be more rounded than that of the EBM. This feature was observed in all pieces and could be linked to a higher heat input from the electron beam source, as reported by Sing et al. [16].

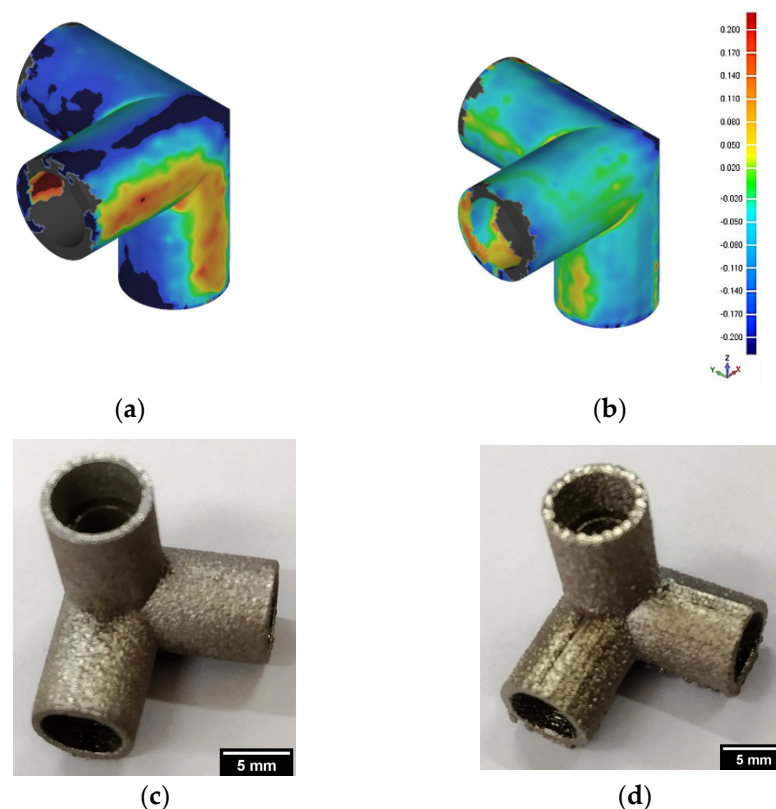


Figure 2. Shapes and dimensions of the connectors: Isometric view of the connector pieces: (a) SLM and (b) EBM. Scale at the right. Actual pieces: (c) SLM and (d) EBM connectors.

The measured average surface roughness (Ra) values in the SLM and EBM parts were $32 \pm 5 \mu\text{m}$ and $42 \pm 6 \mu\text{m}$, respectively. The EBM was slightly rougher than the SLM, as is also visible in Figure 2, perhaps as an indication of the different AM strategies. These values are also below the powder mean diameter ($45\text{--}60 \mu\text{m}$), indicating fusion and consolidation of the impingent added material. The measured roughness values were similar to the layer thickness, indicating that this parameter could influence the resolution and quality of the final product, corroborating the literature [17].

Although slightly different in shape (Figure 2c,d), the samples produced by SLM and EBM showed densifications of $87 \pm 3\%$ and $83 \pm 5\%$, respectively. The density values were similar, indicating that the number of inner pores in the two processes was similar. These densification levels are below those reported for the SLM of pure Ti by Gu et al. (density of 97%) [18] and Ti4Al6V by Yan and Yu (density of 99.7%) [19]. A possible explanation for the low relative densification in both cases may be the methodology used to prepare the connectors in the AM equipment for prostheses. As the mechanical properties of Ti4Al6V are much better than those of bone, the internal porosity does not affect the performance of the implant. Currently, it is not possible to determine whether the same applies to the CubeSat structure.

Figure 3 shows the real mounted CubeSat structure that is ready to be joined. Independently of the AM route, the entire CubeSat frame weighed $122 \pm 4 \text{ g}$, which is approximately the same mass as the aluminum versions [20]. However, it has superior thermal and mechanical resistance to titanium.



Figure 3. Example of the actual CubeSat structure ready for the welds. Each edge measures 100 mm.

3.2. Spot Welds Characterization

The images in Figure 4a,b were obtained by stereoscopy of the weld spots on the connector end produced by SLM and EBM, respectively. In the images, it can be observed that both spot welds have a diameter of approximately 2 mm, and there is a recess in the center of the weld spots. As the weld solidification process started at the border and the grain growth was directed to the center, the recess was associated with liquid-to-solid shrinkage. No surface cracks were observed at the weld spots; however, to assess the presence of internal weld discontinuities, a microstructural analysis of the cross-section was performed.

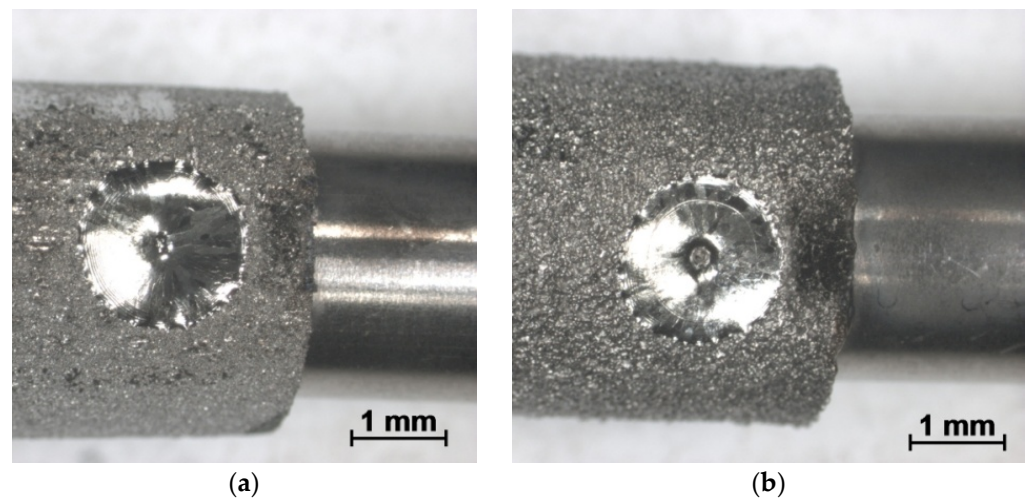


Figure 4. Laser spot welds for superposed connector to tube geometry: (a) SLM and (b) EBM.

Figure 5 shows the micrographs of the cross-sections of the samples produced by SLM (a) and EBM (b) and spot-welded to the grade 2 titanium tube. The fusion zones (FZ), connector side (C), and tube side (T) were marked in the images. In both conditions, isolated spherical pores were observed in the fused zone of the bead weld owing to outgassing [21]. These pores were systematically observed in the weld cross-section, and their location and size indicated the effect of superposed free spacing (gap) as their origin.

In the images of Figure 4a, a depression in the center of the weld bead is observed, as indicated by a white arrow, due to the void formed at the end of solidification, as observed in the images of Figure 3. The presence of the depression did not cause any internal defects owing to the stress concentrator, such as the formation of cracks.



Figure 5. Cont.

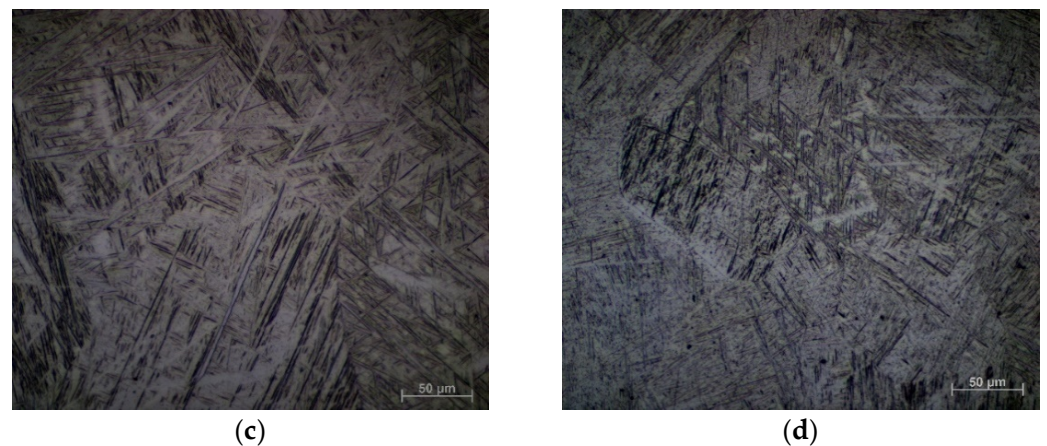


Figure 5. Laser spot welds cross-section macrographs: (a) SLM and (b) EBM. The letters refer to fusion zone (FZ), connector (C), and tube (T). The arrows indicate, approximately, the laser beam optical axis. Micrographs of FZ: (c) SLM and (d) EBM.

Figure 5c,d shows the microstructures of the fusion zones of the weld beads produced by SLM (a) and EBM (b). In both fusion zones, an acicular martensitic microstructure, α' , was observed owing to the high solidification rate (~ 500 °C/s), which is characteristic of laser beam welding [22]. The martensitic transformation starts in the prior β -phase grains and then decorates a fine network of crystallographically oriented plates, in agreement with the literature [23]. This martensitic microconstituent increases the hardness to 750 HV (Vickers hardness) [24].

Figure 6 shows the microhardness profiles of the two laser-welded samples produced via SLM and EBM. The microhardness profile began in the AM connectors, ran through the weld bead, and ended in a grade 2 titanium tube (CP-Ti). In general, both the SLM and the EBM cases showed the same profile; the HV started at approximately 420 HV in the connector, then decreased to a path around 340 HV in the fusion zone, and finally dropped to 130 HV in the tube. The sudden drop in hardness in the region between the fusion zone and the tube could eventually configure a stress concentrator zone.

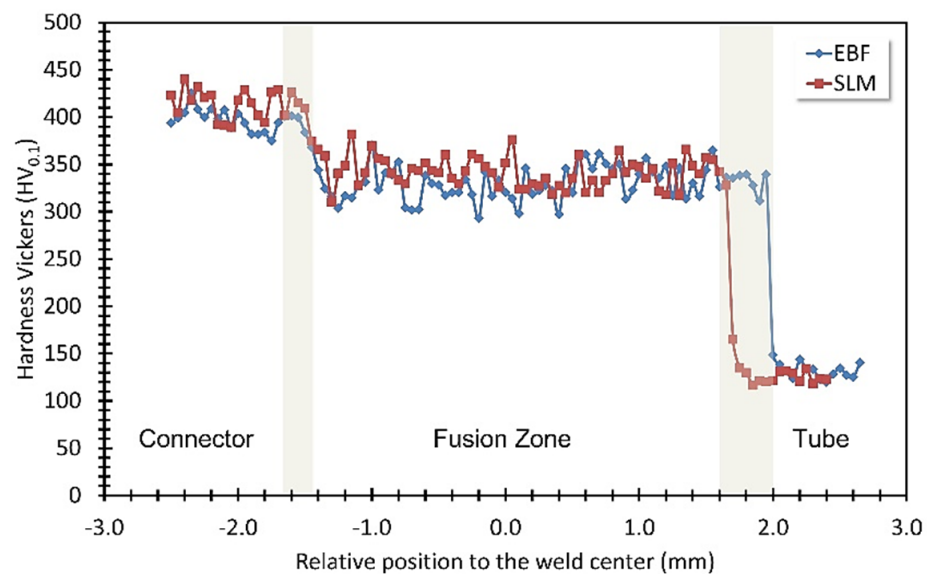


Figure 6. Vickers hardness values as a function of the weld center distance for SLM and EBM cases. Each region is noted at bottom.

Figure 7 shows three representative curves of tensile force versus displacement for specimens SLM and EBM and, for comparison purposes, the F(d) curve for the titanium

tube. As can be seen in the figure, the behavior of the welded assemblies differs significantly from the result obtained when the titanium tube was tested separately. This indicates that rupture occurs at the interface between the connector end and the tube long before permanent deformation of the tube occurs. After three tensile tests, the maximum forces were 2114 ± 420 and 2021 ± 493 N for the SLM and EBM specimens, respectively. Although these values are approximately 33% of the maximum force observed in the tube (~ 6090 N), the results indicate that each connector-tube weld resists a static load of approximately 200 kgf. These tensile strength levels corroborate those reported by Kahraman [25] for electrical discharge spot-welded Ti. Compared to a popular alloy in CubeSat construction, the AA7075-T6 aluminum alloy would need to be three times thicker to withstand this level of stress [26]. Regarding deformations, there was also a significant reduction in the maximum deformation of the tube. In both the LBF and the EBF cases, there was a maximum extension of approximately 2 mm.

From the current perspective, these values are sufficiently large to resist loading during launching in a typical rocket. According to a Brazilian flight record, the maximum speed is 2071 m/s, attaining an acceleration of 13 g at 25.3 of altitude. This should be the maximum hydrostatic pressure, because the maximum acceleration for the 1st stage is 7.7 g decreasing continually up to the apogee (264.5 km). For example, considering that the whole CubeSat weighs half a kilogram, at 13 g the overall load could be 60 N when the cube was coplanar to the baseplate. The maximum loading during launching was only 3% of the ultimate force of failure for every connector-to-tube joint.

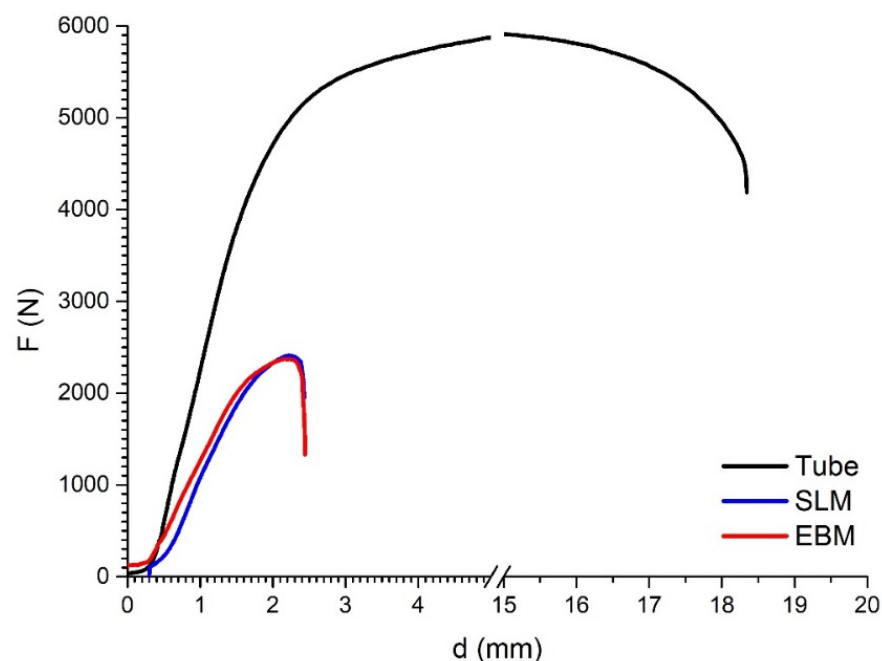


Figure 7. Tensile force (F) versus displacement (d) for two representative cases of SLM and EBM and for the unwelded base Ti tube.

The images in Figure 8 show the fracture surfaces of the SLM (a) and EBM (b) specimens after tensile testing. Looking at both images, similar fracture surfaces were observed, with a region of deformation bounded by the red dotted lines. As the connector and weld nugget had higher hardness values (Figure 6), only the region of the tube adjacent to the weld deformed. The arrows in Figure 8 show the fracture surface, indicating that the weld zone was detached from the tube as the difference in hardness values was high at the interface between the fusion zone and the tube as a stress concentrator. The same failure procedure was reported in other superposed spot-weld tensile tests [27].

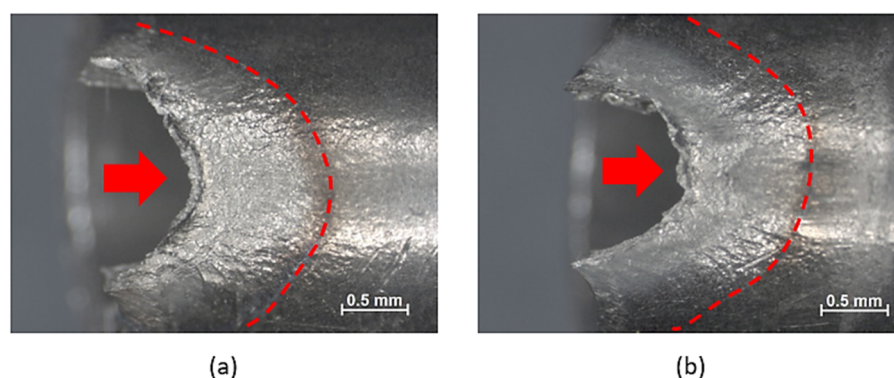


Figure 8. Fractured surfaces after tensile test for two representative cases: (a) SLM and (b) EBM.

4. Conclusions

Titanium CubeSat structures were successfully built using pure titanium tubes and Ti6Al4V connectors obtained by additive manufacturing. Selective laser melting (SLM) and electron beam melting (EBM) techniques were used to manufacture the connectors. For the union between the connectors and tubes, in order to form the structure of the CubeSat, laser beam welding (LBW) was performed.

The produced parts showed a similarity to the planned electronic model, with a maximum deviation of 0.2 mm and a surface roughness R_a of $32 \pm 5 \mu\text{m}$ and $42 \pm 6 \mu\text{m}$ for SLM and EBM, respectively.

An energy of 400 J with a pulse duration of 400 ms from a fiber laser was sufficient for the union between the connectors and the tubes in the present configuration.

The microstructure of the fused zone showed the characteristics of a martensitic microconstituent with a hardness of approximately 320 HV, which was slightly below the hardness of the base material of the connector. At the interface between the weld zone and the tube, there was a sharp decrease in hardness, from 320 to 130 HV, which caused a rupture in this region in the tensile tests.

In terms of load, each laser spot weld averaged 2000 N, which was far above the hydrostatic load in a given rocket launch (60 N). Thus, the CubeSat frame is ready for further robustness and reliability tests.

Author Contributions: Conceptualization, R.H.M.d.S. and D.J.C.; methodology, R.H.M.d.S.; validation, R.H.M.d.S. and D.J.C.; formal analysis, R.H.M.d.S.; investigation, M.S.F.d.L.; resources, M.S.F.d.L.; data curation, R.H.M.d.S. and D.J.C.; writing—original draft preparation, M.S.F.d.L.; writing—review and editing, M.S.F.d.L. and D.J.C.; supervision, M.S.F.d.L. and D.J.C.; project administration, M.S.F.d.L. funding acquisition, M.S.F.d.L. and D.J.C. All authors have read and agreed to the published version of the manuscript.

Funding: This research was funded by São Paulo Research Foundation (FAPESP), grant number 2019/25229-7. This study was financed in part by the Coordenação de Aperfeiçoamento de Pessoal de Nível Superior—Brasil (CAPES)—Finance Code 001.

Data Availability Statement: Not applicable.

Acknowledgments: Thanks are due to BioFabris National Institute for fabricating the AM connectors.

Conflicts of Interest: The authors declare no conflict of interest.

References

1. Space Industry Is on Its Way to \$1 Trillion in Revenue by 2040. Available online: <https://www.cnbc.com/2022/05/21/space-industry-is-on-its-way-to-1-trillion-in-revenue-by-2040-citi.html> (accessed on 26 October 2022).
2. Nanosats Database—Constellations, Companies, Technologies and More. Available online: <https://www.nanosats.eu/> (accessed on 22 October 2022).
3. Levchenko, I.; Bazaka, K.; Belmonte, T.; Keidar, M.; Xu, S. Advanced Materials for Next-Generation Spacecraft. *Adv. Mater.* **2018**, *30*, 1802201. [[CrossRef](#)] [[PubMed](#)]

4. CubeSat Structural Frame—NanoAvionics. Available online: <https://nanoavionics.com/cubesat-components/cubesat-structural-frame/> (accessed on 22 October 2022).
5. McIntosh, D.M.; Baker, J.D.; Matus, J.A. The NASA CubeSat Missions Flying on Artemis-1. Available online: <https://digitalcommons.usu.edu/cgi/viewcontent.cgi?article=4646&context=smallsat> (accessed on 22 October 2022).
6. Morris, D.; Noble, R. CubeSat Advanced Technology Propulsion System Concept. 2014. Available online: <https://digitalcommons.usu.edu/smallsat/2014/Propulsion/2/> (accessed on 22 October 2022).
7. Sacco, E.; Moon, S.K. Additive manufacturing for space: Status and promises. *Int. J. Adv. Manuf. Technol.* **2019**, *105*, 4123–4146. [[CrossRef](#)]
8. Angel, N.M.; Basak, A. On the fabrication of metallic single crystal turbine blades with a commentary on repair via additive manufacturing. *J. Manuf. Mater. Process.* **2020**, *4*, 101. [[CrossRef](#)]
9. Shinde, M.S.; Ashtankar, K.M. Additive manufacturing–assisted conformal cooling channels in mold manufacturing processes. *Adv. Mech. Eng.* **2017**, *9*, 1687814017699764. [[CrossRef](#)]
10. Ampatzoglou, A.; Tsantzalidis, S.; Mazarakos, D.E.; Kostopoulos, V. 3D printed frame for cubesat applications for low-earth orbit mission. *Int. J. Comput. Aided Eng. Technol.* **2017**, *9*, 434–452. [[CrossRef](#)]
11. Rafi, H.K.; Karthik, N.V.; Gong, H.; Starr, T.L.; Stucker, B.E. Microstructures and mechanical properties of Ti6Al4V parts fabricated by selective laser melting and electron beam melting. *J. Mater. Eng. Perform.* **2013**, *22*, 3872–3883. [[CrossRef](#)]
12. Yu, H.; Li, F.; Yang, J.; Shao, J.; Wang, Z.; Zeng, X. Investigation on laser welding of selective laser melted Ti-6Al-4V parts: Weldability, microstructure and mechanical properties. *Mater. Sci. Eng. A* **2018**, *712*, 20–27. [[CrossRef](#)]
13. ASTM C373-18; Standard Test Methods for Determination of Water Absorption and Associated Properties by Vacuum Method for Pressed Ceramic Tiles and Glass Tiles and Boil Method for Extruded Ceramic Tiles and Non-tile Fired Ceramic Whiteware Products. ASTM International: West Conshohocken, PA, USA, 2018.
14. ASTM E407-07(2015)e1; Standard Practice for Microetching Metals and Alloys. ASTM International: West Conshohocken, PA, USA, 2016.
15. Vayssette, B.; Saintier, N.; Brugger, C.; Elmay, M.; Pessard, E. Surface roughness of Ti-6Al-4V parts obtained by SLM and EBM: Effect on the High Cycle Fatigue life. *Procedia Eng.* **2018**, *213*, 89–97. [[CrossRef](#)]
16. Sing, S.L.; An, J.; Yeong, W.Y.; Wiria, F.E. Laser and electron-beam powder-bed additive manufacturing of metallic implants: A review on processes, materials and designs. *J. Orthop. Res.* **2016**, *34*, 369–385. [[CrossRef](#)] [[PubMed](#)]
17. Leary, M. Surface roughness optimisation for selective laser melting (SLM): Accommodating relevant and irrelevant surfaces. In *Laser Additive Manufacturing*; Woodhead Publishing: Sawston, UK, 2017; pp. 99–118.
18. Gu, D.; Hagedorn, Y.C.; Meiners, W.; Meng, G.; Batista RJ, S.; Wissenbach, K.; Poprawe, R. Densification behavior, microstructure evolution, and wear performance of selective laser melting processed commercially pure titanium. *Acta Mater.* **2012**, *60*, 3849–3860. [[CrossRef](#)]
19. Yan, M.; Yu, P. *An Overview of Densification, Microstructure and Mechanical Property of Additively Manufactured Ti-6Al-4V—Comparison among Selective Laser Melting, Electron Beam Melting, Laser Metal Deposition and Selective Laser Sintering, and with Conventional Powder*; IntechOpen: London, UK, 2015.
20. CubeSat Structures—Cubesat Components—SPACEMANIC. Available online: <https://www.spacemanic.com/cubesat-structures> (accessed on 26 October 2022).
21. Huang, J.L.; Warnken, N.; Gebelin, J.C.; Strangwood, M.; Reed, R.C. On the mechanism of porosity formation during welding of titanium alloys. *Acta Mater.* **2012**, *60*, 3215–3225. [[CrossRef](#)]
22. Fan, Y.; Tian, W.; Guo, Y.; Sun, Z.; Xu, J. Relationships among the Microstructure, Mechanical Properties, and Fatigue Behavior in Thin Ti6Al4V. *Adv. Mater. Sci. Eng.* **2016**, *2016*, 7278267. [[CrossRef](#)]
23. Motyka, M. Martensite formation and decomposition during traditional and AM processing of two-phase titanium alloys—An overview. *Metals* **2021**, *11*, 481. [[CrossRef](#)]
24. Omoniyi, P.O.; Akinlabi, E.T.; Mahamood, R.M. Heat treatments of Ti6Al4V alloys for industrial applications: An overview. In *IOP Conference Series: Materials Science and Engineering*; IOP Publishing: Bristol, UK, 2021; Volume 1107, p. 012094.
25. Kahraman, N. The influence of welding parameters on the joint strength of resistance spot-welded titanium sheets. *Mater. Des.* **2007**, *28*, 420–427. [[CrossRef](#)]
26. Sekerere, K.; Mushiri, T. Finite element analysis of a cubesat. In Proceedings of the 2017 International Conference on Industrial Engineering and Operational Management (IEOM), Bristol, UK, 24–25 July 2017.
27. Habib, L.; Abdelkader, Z.; Habib, B.; Benallel, B.F. Experimental study of tensile test in resistance spot welding process. *Lat. Am. J. Solids Struct.* **2016**, *13*, 1228–1235. [[CrossRef](#)]